

Towards Rydberg quantum logic with trapped ions

P. Bachor, T. Feldker, J. Walz, and F. Schmidt-Kaler

QUANTUM, Institut für Physik, Johannes Gutenberg-Universität
Staudingerweg 7, and Helmholtz-Institut Mainz, Johann-Joachim-Becherweg 36,
D-55128 Mainz, Germany

E-mail: bachor@uni-mainz.de

Abstract. We demonstrate the excitation of ions to the Rydberg state $22F$ by vacuum ultraviolet radiation at a wavelength of 123 nm combined with the coherent manipulation of the optical qubit transition in $^{40}\text{Ca}^+$. With a tightly focused beam at 729 nm wavelength we coherently excite a single ion from a linear string into the metastable $3D_{5/2}$ state before a VUV pulse excites it to the Rydberg state. In combination with ion shuttling in the trap, we extend this approach to the addressed excitation of multiple ions. The coherent initialization as well as the addressed Rydberg excitation are key prerequisites for more complex applications of Rydberg ions in quantum simulation or quantum information processing.

PACS numbers: 37.10.Ty, 32.80.Ee, 42.50.Ex

Contents

1	Motivation for Rydberg excitations in trapped ion crystals	1
2	Description of the experimental setup	2
2.1	Linear segmented ion trap for Calcium ions	2
2.2	Laser sources for optical cooling and detection	4
2.3	Individual ion addressing on the optical qubit transition	5
2.4	Vacuum ultra violet source near 123 nm	6
2.5	Vacuum ultra violet beam delivery to trapped ion crystal	8
3	Experimental results on the $22F$ Rydberg excitation	8
3.1	Zeeman-state selective qubit initialization and Rydberg excitation	9
3.2	Addressing single ions in a linear crystal	11
4	Conclusion	14

1. Motivation for Rydberg excitations in trapped ion crystals

Trapped cold ion crystals have multiple applications in fundamental and applied science. This includes sophisticated processes in quantum simulation and quantum information applications [1, 2, 3]. Core elements are two-qubit quantum logic operations, implemented by spin-dependent light forces on ions, which are conveyed

along the entire Coulomb crystal [4]. Quantum algorithms such as the Shor factorization algorithm [5] and elementary quantum simulations of spin-dynamics [6, 7] have been implemented. Such progress demonstrates the versatility of two-qubit gate operations, historically starting from the Cirac-Zoller gate [4, 8], the Moelmer-Soerensen gate [9, 10] or the geometric phase gate [11]. On the other hand, impressive results are reported in the research area of Rydberg quantum logic operations [12, 13, 14, 15] and Rydberg many-body-physics, where the giant dipolar interactions are exploited to simulate quantum spin-models [16, 17, 18], or investigate the role of impurities in quantum systems.

Here, we present our experimental approach to join the advantages of ion crystals for quantum information processing, thus implementing an optical addressable single qubit in a linear register, with Rydberg excitations and the corresponding giant dipolar forces. The interplay between Coulomb and Rydberg interactions will enable fast multi-qubit gate operations [19] and might also allow for the observation of novel many-body phenomena [21] or non-equilibrium dynamics of such systems [20].

We exemplify our case by an addressed Rydberg excitation on the $3D_{5/2}$ to $22F$ transition in cold trapped Calcium ions at 123.256119(5) nm wavelength. The article starts describing the experimental apparatus which includes a segmented ion trap, and lasers to initialize and manipulate the optical qubit on the $4S_{1/2} \leftrightarrow 3D_{5/2}$ transition in $^{40}\text{Ca}^+$. We describe an optical assembly which allows for single ion addressing [22] on the optical qubit transition, in combination with optical access for the VUV-laser beam which is used to drive the Rydberg excitation. We demonstrate the selective state preparation of single ions in a linear crystal, and the subsequent excitation to the $22F$ Rydberg state. Recently, we have reported the excitation of higher lying F states with principal quantum numbers $n > 50$ and presented a systematic study of the effects of large electric polarizabilities for such states [23]. The combination of coherent manipulation of qubits with the excitation to Rydberg levels, as demonstrated in this publication, will be the key for designing the Rydberg-interactions and quantum gate operations. We discuss future challenges and plans in the conclusion.

2. Description of the experimental setup

In this section we describe the experimental setup for the Rydberg excitation of $^{40}\text{Ca}^+$ ions. First, we explain the design of the segmented linear Paul trap and the integration of the laser beam at 729 nm wavelength. Furthermore, we describe the generation of narrow band and continuous wave (cw) vacuum ultraviolet radiation near 123 nm wavelength and the beam delivery to the ion crystal.

2.1. Linear segmented ion trap for Calcium ions

For the confinement of the ions a linear Paul trap with segmented electrodes is used. The blades for the segmented electrodes are fabricated from a $125\ \mu\text{m}$ thick wafer of alumina substrate cut with femtosecond laser pulses. Ceramic parts get a 300 nm evaporated gold coating. They are glued to a titanium frame such that they form a X-shaped linear trap with $480\ \mu\text{m}$ distance from electrode surfaces to the symmetry center. A radio frequency (RF) voltage is applied to two diagonally opposing blades to generate the radial potential. The RF voltage comes by a signal generator *, an

*HP-8657B Signal Generator

analog attenuator * allows for fast adjustment of the RF-amplitude, followed by a power amplifier †. A helical resonator is used for impedance matching of the amplifier output with the ion trap circuit. We have operated two different helical resonators with resonance frequencies $\Omega_{\text{RF}}/2\pi = 6.5 \text{ MHz}$ or $\Omega_{\text{RF}}/2\pi = 20 \text{ MHz}$, respectively. An amplitude of up to $U_{\text{RF}} = 200 \text{ V}$ results in radial vibrational secular frequencies $\omega_{\text{rad}}/2\pi = 700 \text{ kHz} - 2 \text{ MHz}$.

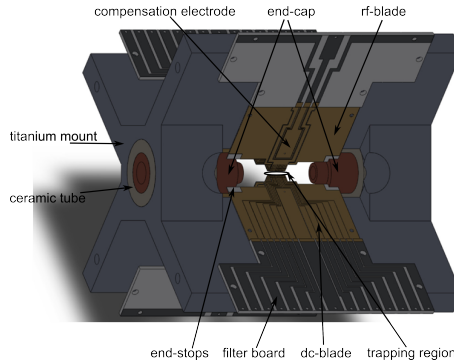


Figure 1. Construction drawing of the segmented Paul trap. The trap electrodes are made from gold coated ceramic blades, glued to an X-shaped titanium mount. See text for more details.

The trap is designed (Fig. 1 and Ref. [24]) to optimize the accuracy of the radial alignment of all four blades with respect to the symmetry trap axis, thus minimizing micro-motion. Differential charging of the surfaces and residual imperfections of the device are compensated by correction voltages to center the ions at the RF-node. Compensation electrodes are placed behind the RF rails on the respective blades. We operate these electrodes with voltages of $\pm 10 - 100 \text{ V}$, generated by DC/DC converters‡ with additional low pass filters, controlled by the analogue output (AO) of a NI card §.

The DC blades are segmented in 11 electrodes, each of width $180 \mu\text{m}$, separated by a $30 \mu\text{m}$ insulation gap. Over the 11 segments the total length of the DC-blades is 2.28 mm . DC-voltages are fed to each of the electrodes, to generate the axial confinement. Additionally, two steel-cones, with a center-pierced hole of $750 \mu\text{m}$ radius are mounted at a distance of 12 mm on the symmetry axis. They are electrically insulated and can act as DC-end caps of the trap. The holes provide axial optical access for the vacuum ultra violet (VUV) radiation.

Each DC segment is connected via a CLC-filter with 50 kHz cutoff frequency to a home-built multi-channel voltage source; a FPGA controlled device which delivers ultra low noise arbitrary waveforms in 4×12 parallel channels with an update rate of 400 ns and a range of $\pm 10 \text{ V}$. This setup allows for the generation of customized axial potentials according to the various experimental requirements, as well as fast shuttling [25] and separation [26] of ion crystals without thermal excitation. We generate axial potentials of $\omega_{\text{ax}}/2\pi = 250 \text{ kHz} - 900 \text{ kHz}$.

The quantization axis for the optical transitions is provided by a magnetic field

*mini circuits ZX73-2500

†mini circuits ZHL-5W-1, 5 W

‡HighTek; PM12-100±

§National instruments; PCI-6703

with an angle of $\pi/4$ to the trap axis. The vacuum vessel admits for optical access parallel, perpendicular and with an angle of $\pi/4$ to the trap axis, see Fig. 3. We briefly describe the laser sources in the following. The vessel is evacuated by a NEX Torr D 100-5 pump to about 10^{-11} mbar.

2.2. Laser sources for optical cooling and detection

Calcium atoms from a resistively heated oven are ionized with light near 423 nm and 375 nm. Ions are excited with light-fields near wavelengths of 393 nm, 397 nm, 854 nm and 866 nm. We employ grating stabilized diode lasers in Littrow configuration. Two commercially available Toptica DL pro lasers at wavelength of 393 nm* and 397 nm† and two home built lasers at 854 nm‡ and 866 nm§ wavelength provide an optical output power of about 10 mW each. All wavelengths are monitored by a wavelength meter¶. The lasers at 397 nm and 866 nm wavelength are stabilized to a medium finesse cavity using a Pound-Drever-Hall (PDH) locking scheme. A laser line-width well below 1 MHz is reached.

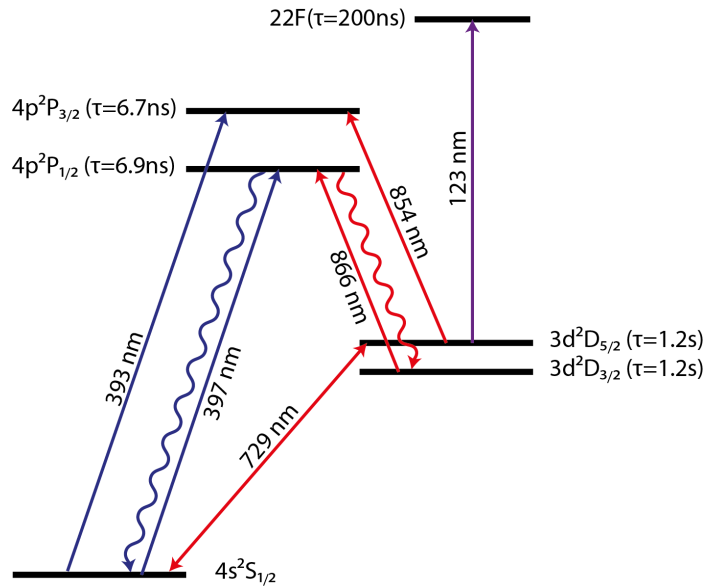


Figure 2. Levels and transitions in Calcium Laser sources near 432 nm and 375 nm are used for the two photon ionization of Calcium, sources near 393 nm, 397 nm, 866 nm, and 854 nm are employed for driving the dipole transitions in Ca^+ , see text for details. The Rydberg state is excited from the long lived $3D_{5/2}$ state.

The laser beams are switched by acousto-optic modulators|| (AOMs) ensuring fast switching times $< 1 \mu\text{s}$ and high repetition rates needed for the experiment. The light is delivered to the experiment by single mode polarization maintaining fibers and the

*LD-0395-0120-1, 13mW; Toptica

†LD-0397-0030-1, 13mW; Toptica

‡HL8342MG, 50mW, 852nm; opnext

§LD-0870-0100-2, 100mW; Toptica

¶wavelength meter WSU-10 (infrared) and wavelength meter WSU-7 (blue); Toptica

||BRI-QFZ-80-20-395 (blue) and BRI-TEF-80-20-860 (infrared); Brimrose

beams are focused onto the ions with the fiber coupling optics. Relevant levels and transitions of $^{40}\text{Ca}^+$ are shown in Fig. 2.

Ions are detected by imaging their fluorescence at 397 nm wavelength to an electron multiplied charged coupled device (EMCCD) camera*. A magnification of $m = 17.7(1.4)$ of the imaging system is chosen and we fully resolve the fluorescence of individual ions in linear and planar ion crystals, where the inter-ion distances are a few μm .

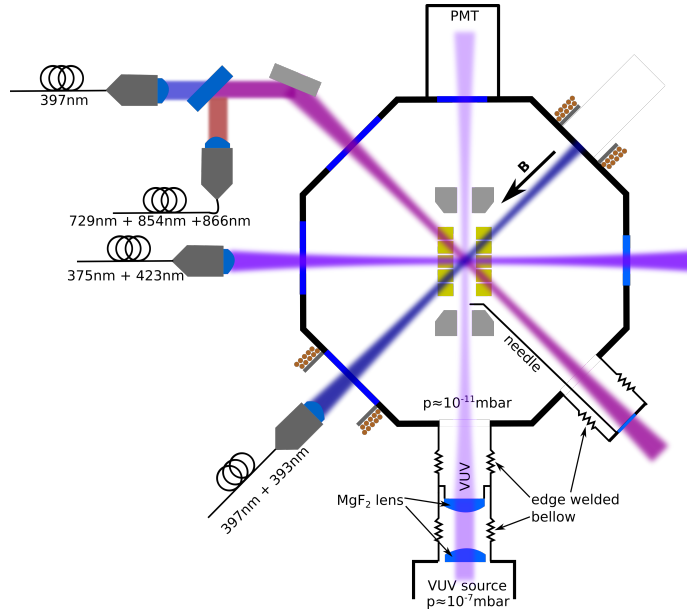


Figure 3. Optical access of the Paul trap. Directions of laser-beams and magnetic field in the ion trap viewed from the top. The VUV beam propagates axially through the trap, focused by two MgF_2 lenses. Beams for Doppler cooling and optical pumping are delivered to the vacuum vessel by optical fibers and propagate parallel and perpendicular to the magnetic field, featuring a projection on the x, y, and z axis of the trap. The light at 729 nm wavelength is superimposed with the Doppler beam, in the beam path (a) and used for globally illuminating the ion crystal with coupling to all motional modes.

2.3. Individual ion addressing on the optical qubit transition

The qubit information is carried in a single ion in two long-lived electronic states, namely the ground state and the metastable $3D_{5/2}$ level. To manipulate the optical qubit transition in $^{40}\text{Ca}^+$, we employ a Titanium:Sapphire laser †, operated at 729 nm wavelength and frequency stabilized [27] to a high finesse ultra-stable reference cavity ‡. We estimate a linewidth of better than 100 Hz. The spectrally narrow radiation is used for resolved sideband cooling as well as individual coherent excitation of ions. The light is delivered to the experiment by a 100 m long single mode fiber, hence fiber noise cancellation is employed to preserve the spectral purity of the light. We use

*Andor; IXon3 897; 512×512 pixel; pixel size $16 \times 16 \mu\text{m}$

†Matisse TX; Sirah, pumped by Millennia Pro 15s; Spectra Physics

‡6020 notched cavity $F = 140000$; ATFilms

an AOM operated at 110 ± 15 MHz, in double pass configuration for switching, pulse shaping and frequency tuning of the light. Two different beam paths (denoted (a) and (b)) deliver the light pulses to the ion crystal. For (a), the beam is coupled into the same fiber as the IR beams (854 nm and 866 nm), propagates through the trap perpendicular to the magnetic field and has a projection on all principal axes of the trapping potential. With a spot size of $50 \mu\text{m}$ this beam illuminates the whole ion crystal. Rabi frequencies in the order of $\Omega/2\pi = 100$ kHz are achieved with an optical power of 15 mW. For path (b) the 729 nm radiation is coupled into a separate single-mode and polarization-maintaining fiber, overlapped with the ion's fluorescence image, and focused* to a spot size of $\omega_0 = 4 \mu\text{m}$. Due to the high intensity in the tight focus we achieve Rabi frequencies around $\Omega/2\pi = 1$ MHz. This beam propagates vertically, perpendicular to the trap axis and is used to address single ions, see Fig. 4. We will describe the corresponding experimental results in Sect. 3.2.

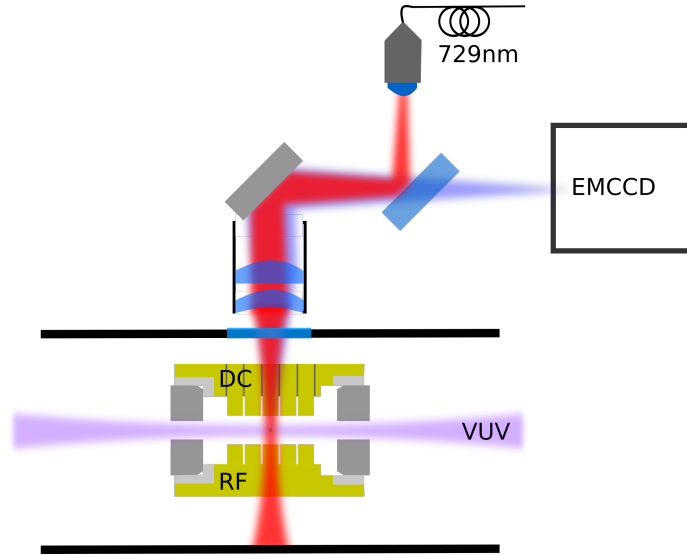


Figure 4. The light path of the single ion addressing beam. The light at 729 nm wavelength is irradiated vertically into the trap on the beam path (b), superimposed on the fluorescence image, tightly focused by a lens with high numerical aperture. The fluorescence image is detected with an EMCCD camera. The two end caps allow for precise radial alignment of the blades. The segmented electrodes are separated by insulation gaps.

2.4. Vacuum ultra violet source near 123 nm

The coherent VUV light near 123 nm wavelength is generated in a nonlinear four-wave mixing process in mercury vapor. A triple-resonant scheme is implemented; laser beams at 254 nm, 408 nm and 580 nm wavelength are superimposed via dichroic mirrors and focused into a mercury vapor cell. The mixing efficiency $\epsilon \propto |\chi^{(3)}|^2$ ranges between 20 and $30 \mu\text{W}/\text{W}^3$ at the required excitation wavelength, where $\chi^{(3)}$ denotes the third order nonlinear susceptibility. For a strong enhancement of $\chi^{(3)}$

*Sill Optics; focal length $f=66.8$ mm, aperture $D=38$ mm, for 397 nm and 729 nm wavelength

the frequencies of the three fundamental radiation fields are tuned in the vicinity of atomic resonances in mercury [28].

A schematic illustration of the laser setup is shown in Fig. 5. The ultraviolet light

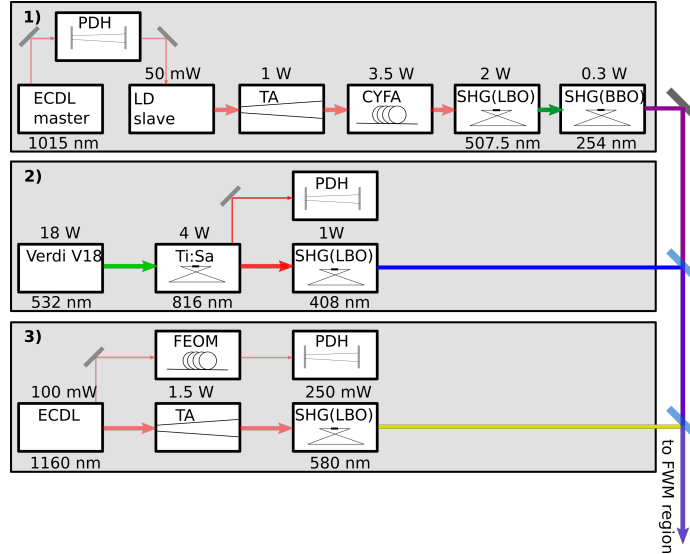


Figure 5. Block diagram of the lasers used to create the fundamental light fields at 254 nm (top), 408 nm (middle), and 580 nm (bottom) wavelength for the FWM process. The light is generated by frequency-doubling (quadrupling) the output of high power infrared lasers. Frequency stabilization to medium finesse cavities ensures narrow spectral bandwidth of the outgoing light. ECDL denotes the external cavity diode lasers, TA stands for tapered amplifier, the frequency servo uses a Pound-Drever-Hall (PDH) scheme, (C)YFA denotes the (cryogenic) ytterbium fiber amplifier and frequency doubling (SHG).

at 254 nm wavelength is produced by the amplified and frequency-quadrupled output of a grating stabilized laser diode at 1015 nm wavelength. We employ a master/slave diode laser system: The master diode's output is stabilized to a medium finesse cavity, the transmitted light is used for injection-locking of the slave diode. Hence, a narrow linewidth of about 60 kHz is achieved. After the cryogenic fiber amplifier [29] and the two frequency doubling stages we end up with a typical power of about 200 mW. The beam is focused to a waist size of $\omega_0 \approx 6 \mu\text{m}$ in the center of the mercury mixing region.

The output of a stabilized Titanium:Sapphire laser at 816 nm wavelength is frequency-doubled, to generate 1 W of light at 408 nm wavelength. We obtain a linewidth of about 30 kHz and measure a spot size of $\omega_0 \approx 14 \mu\text{m}$ at the center of the mixing cell.

These two fundamental light fields are fixed at an optimal wavelength for the nonlinear process. The third fundamental is tuned such that the resulting VUV wavelength matches the resonance conditions to excite the Rydberg transition in $^{40}\text{Ca}^+$. A high power laserdiode* at 1160 nm wavelength is operated in an external

*Innolume GC-1160-90-TO-200-A

cavity in Littrow configuration. A high bandwidth fiber EOM* modulates the light, generating sidebands at a computer controlled frequency. Stabilizing the frequency of one sideband to the resonance of the cavity allows for mode-hop-free frequency scanning of the laser in a range of ± 1 GHz, and results in a spectral width of ≈ 80 kHz. About 80 mW of this light is injected into a tapered amplifier†. For frequency doubling we use a LBO crystal in an enhancement bow-tie cavity. We generate an output power of 250 mW at 580 nm wavelength. The beam waist in the mercury vapor is determined as $\omega_0 \approx 13 \mu\text{m}$ for optimized VUV generation.

We determine frequencies of all fundamental waves with a wavelength meter‡. The frequency fluctuation of the generated VUV light is the sum of the fundamental spectral linewidths, resulting in a linewidth $\Gamma_{\text{VUV}} < 500$ kHz. We monitor the power of the VUV light transmitted through the trap with a photomultiplier.

2.5. Vacuum ultra violet beam delivery to trapped ion crystal

A major challenge is the connection between the VUV source and the ion trap. Light at 123 nm wavelength is absorbed by air, thus vacuum conditions are necessary for the complete beam path. The apparatus is sketched in Fig. 3. The beam is focused into the trap by a telescope which consists of two MgF_2 lenses. The second of the two lenses is glued airtight to a titanium mount in between two flexible bellows and separates the VUV generation zone with a pressure of about 10^{-7} mbar from the ion trap's vacuum ($\sim 10^{-11}$ mbar).

For a coarse alignment of the VUV beam, the ion trap's vacuum vessel is moved with respect to the VUV source and the power transmitted through the trap is optimized. For fine-adjustment, we move a needle tip into the trap and observe the transmitted VUV power on a photomultiplier which is placed behind the trap. We determine the trap center by observing the ion's fluorescence on the EMCCD camera, and adjust the needle's position accordingly. The VUV beam is adjusted to the needle tip's position by moving the second lens of the telescope which is fixed to a 2D-translation stage. The VUV beam is focused into the trap with $\omega_0 \approx 11 \mu\text{m}$ passing the holes in the end caps. Including transmission losses from optical elements in front of the trap we obtain $P_{\text{VUV}} \approx 10 - 80$ nW at the ion.

3. Experimental results on the $22F$ Rydberg excitation

In a recent publication [23] we have presented the excitation of Rydberg F states with $n > 50$ from the $3D_{3/2}$ state which has been populated by incoherent optical pumping. In the experiments presented here, however, we initialize the D-level by a coherent excitation on the $4S_{1/2} \leftrightarrow 3D_{5/2}$ transition. The upper qubit level is precisely the initial state for Rydberg excitation. In this section we present two examples for the toolbox opened up by the combination of Rydberg excitation of ions and coherent operation on long-lived electronically low lying qubit states: The first subsection attends to the initialization of the ion with a π -rotation into specific Zeeman states of the $3D_{5/2}$ followed by Rydberg excitation with VUV radiation. In the second part we demonstrate individually addressed Rydberg excitation of one and two ions in a linear Coulomb crystal. Beyond the initialization in the upper qubit level

*Photline NIR-MPX-LN-10 driven by R&S SMP03 signal generator

†BoosTA pro, 1.5 W

‡HighFinesse WSU 10

$3D_{5/2}$, the integration of narrow bandwidth radiation at 729 nm into the setup has further benefits. Resolved sideband spectroscopy allows for a precise determination of the ions motional state, in regard to the thermal motion and the driven micro-motion (see Fig. 6). This is essential, as both effects do affect the line shape of the Rydberg transition. Furthermore, by using the narrow quadrupole transition near 729 nm for by resolved sideband cooling we can be prepare the ion motion close to the vibrational ground state.

Here, we combine Rydberg excitation to the $22F$ state at a wavelength of $\lambda_{22F} = 123.256119(5)$ nm with coherent manipulation of the optical qubit in $^{40}\text{Ca}^+$. This is a key prerequisite for the use of Rydberg dipole-dipole interaction for generating multi-particle entanglement of ions.

3.1. Zeeman-state selective qubit initialization and Rydberg excitation

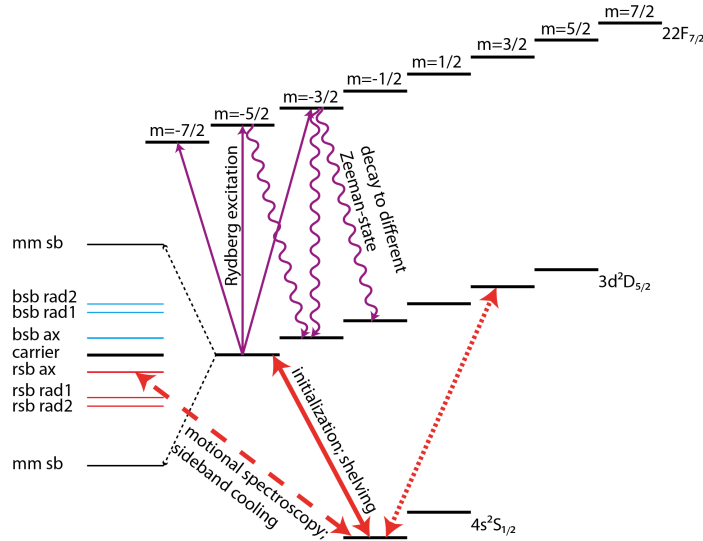


Figure 6. Zeeman structure of the energy levels used in the Rydberg excitation. The ion is initialized by a π -rotation on the $|4S_{1/2}, -1/2\rangle \leftrightarrow |3D_{5/2}, -5/2\rangle$ transition (solid red arrow). Alternatively the ion can be initialized in other Zeeman states (red dotted arrow). Individual Zeeman transitions are resolved due to the sharp resonance of this transition. Subsequently the ion is excited to the $22F$ state. Individual Zeeman transitions are not resolved in this step as the Rydberg resonance is broadened by the thermal motion of the ion and the linewidth of the VUV laser to about 3 MHz. The excitation, followed by a decay back to the $3D_{5/2}$ state can change the Zeeman state. A second π -rotation is applied on the original $|4S_{1/2}, -1/2\rangle \leftrightarrow |3D_{5/2}, -5/2\rangle$ transition, which rotates solely the population of the initial Zeeman state back to the ground state. Additionally the $4S_{1/2} \leftrightarrow 3D_{5/2}$ transition is used for precise spectroscopy of the magnetic field, as well as the thermal and driven (micro) motion of the ion (red dashed arrow). Resolved sideband cooling on this transition brings the ion close to the thermal ground state.

The magnetic field which we apply in the experiment lifts the degeneracy of Zeeman-states by $E_z = \mu_B \cdot g_j \cdot B$. Due to the narrow resonance of the $4S_{1/2} \leftrightarrow 3D_{5/2}$ transition, individual Zeeman-states can be excited. After side band cooling and

optical pumping to the $|4S_{1/2}, \pm 1/2\rangle$ state, we reach about 90% population transfer to the desired $|3D_{5/2}, m\rangle$ state, with a single π -rotation. In contrast to the sharp $4S_{1/2} \leftrightarrow 3D_{5/2}$ resonance, the resonance width for the transition to the Rydberg $22F$ state is much broader due to the comparatively short lifetime of this state ($\tau = 200$ ns [30]), the thermal motion of the ion and the linewidth of the VUV radiation. In the $F_{7/2}$ manifold a magnetic field of $B = 0.28$ mT yields a frequency splitting of 4.5 MHz. Consequently we do not resolve the individual Zeeman-states of the $22F$, but the VUV radiation at 123.256119(5) nm wavelength induces transition with $\Delta m = -1, 0, 1$. Together with a subsequent decay back to the $3D_{5/2}$ state (again subjected to the selection rule $\Delta m = -1, 0, 1$), this results in a population transfer out of the initial Zeeman-state which indicates successful excitation.

The new measurement sequence is based on fluorescence detection which allows for discriminating between the $3D_{5/2}$ state (no emitted photons - dark ion) and the $4S_{1/2}, 3D_{3/2}$ states (continuous fluorescence - bright ion) with high-fidelity. We use additional laser pulses to measure the population transfer between Zeeman levels, induced by the excitation to the Rydberg state. a) Ions are initialized with a π -pulse on the $|4S_{1/2}, \pm 1/2\rangle \leftrightarrow |3D_{5/2}, \pm 5/2\rangle$ transition. b) A VUV pulse of 1.5 ms excites ions to the Rydberg states, from where they decay rapidly back to the $3D_{5/2}$. c) A π -pulse on the $|4S_{1/2}, \pm 1/2\rangle \leftrightarrow |3D_{5/2}, \pm 5/2\rangle$ transition rotates population that did not change the Zeeman state back to the ground state. d) Optical pumping with light at 397 nm, hides the ground state population in the $3D_{3/2}$ state. e) An additional pulse on the $|4S_{1/2}, \pm 1/2\rangle \leftrightarrow |3D_{5/2}, \pm 5/2\rangle$ transition increases the fidelity of the shelving further to $> 95\%$. f) Light at wavelength of 397 nm and 866 nm is switched on for the fluorescence detection. The complete sequence is shown in Fig 7. As compared to the detection technique which we used in our previous experiments [23], where we observe a change in the total angular momentum j as the Rydberg state is excited and decays back to the D state, this new method is more efficient by about a factor of 5. This enabled us to reduce the VUV-pulse time to 1.5 ms.

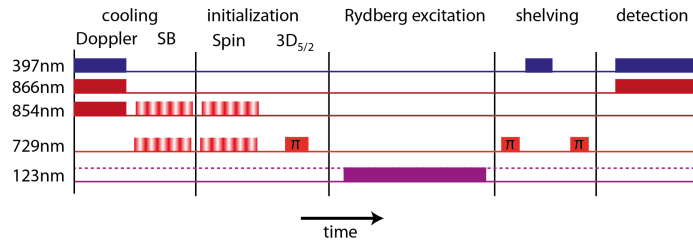


Figure 7. Pulse sequence used for excitation of different Zeeman states. During the initialization sequence the ions are excited into the $3D_{5/2}$ state via π -pulses. The shelving sequence prepares for the fluorescence detection of Rydberg excitation.

The data presented in Fig. 8a shows the transition resonances for either the initial state $|3D_{5/2}, +5/2\rangle$ or $|3D_{5/2}, -5/2\rangle$. The resonances are composed of transitions to two Zeeman states each, with $\Delta m = \{0, 1\}$ and $\Delta m = \{-1, 0\}$ (see Fig 8b). The observed frequency shift of 5 MHz corresponds to the asymmetric excitation and detection scheme and an additional contribution of 1.1 MHz from the different g_j factors of $g_j(D_{5/2}) = 6/5$ and $g_j(F_{7/2}) = 8/7$. The experimentally determined resonances agree with a model function consisting of Gaussian distributions with

$\sigma = 3.8$ MHz for each Zeeman transitions if we take into account a magnetic field of $B = 0.28$ mT. The strength of the magnetic field has been precisely measured by spectroscopy on the $4S_{1/2} \leftrightarrow 3D_{5/2}$ transition.

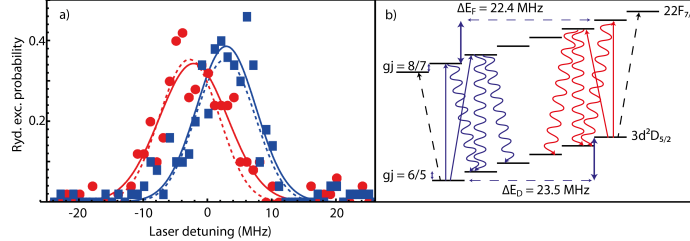


Figure 8. Experimental data of the excitation resonance of the $22F$ state from $3D_{5/2}$ $m = -5/2$ (blue) and $m = 5/2$ (red). a) Solid lines represent a fit of a Gaussian distribution to the experimental data, the linewidth from the fit are $\sigma = 5.3$ MHz (red) and $\sigma = 4.6$ MHz (blue) respectively. The separation of 5 MHz agrees well with a model function (dashed lines) b). Illustration of the possible decay channels, after excitation from $|3D_{5/2}, -5/2\rangle$ (blue) and $|3D_{5/2}, 5/2\rangle$ (red). The excitation to $|22F, \pm 7/2\rangle$ can not be detected as the only decay channel is back to the initial state.

3.2. Addressing single ions in a linear crystal

For advanced applications in quantum simulation or quantum computing it will be necessary to excite specific ions out of large Coulomb crystals. Here, we demonstrate the single ion addressing of Rydberg excitation. Instead of addressing single ions with a focused and steered VUV-beam, we initialize selected ions to the $3D_{5/2}$ state with the tightly focused beam at 729 nm wavelength - only those ions will undergo excitation to the Rydberg level, even though the beam near 123 nm is illuminating the entire ion crystal. This concept has important advantages: The $3D_{5/2}$ state lives for $\tau = 1168(9)$ ms [31] such that we have sufficient time for pulses and transport or separation sequences to initialize and configure multiple ions before a single VUV pulse excites all D-state ions at once. Furthermore, it appears to be technically straight forward to address ions with a laser beam at 729 nm wavelength while it would be much more challenging to rapidly steer on single ions with a VUV beam.

For this experiment we changed the trap drive radio frequency to $\Omega_{RF}/2\pi = 20$ MHz (see Sect. 2.1) in order to generate a more stable potential for multiple ions. Vibrational frequencies of $\omega_{rad}/2\pi = 1.5$ MHz and $\omega_{ax}/2\pi = 600$ kHz were obtained, which corresponds to an inter ion distance of $d \approx 7 \mu\text{m}$.

The pulse sequence used for the addressed excitation of one ion, or two ions, in a crystal of three ions is illustrated in Fig. 9. a) Two π -pulses on different Zeeman transitions are used for the initialization of each ion in order to increase the population transfer to $> 90\%$. b) A VUV pulse of ≈ 5 ms excites the ions on the $3D_{5/2} \rightarrow 22F$ transition, a fraction of the excited ions decay to the $3D_{3/2}$ state. c) ground state population of all ions is pumped to the $3D_{5/2}$ state with 90% fidelity. d) Thus, the initialized and the non-initialized ions are in the dark state ($3D_{5/2}$), only ions excited to Rydberg states and decayed to the $3D_{3/2}$ scatter photons during illumination with light at 397 nm wavelength. With this scheme we avoid the use of addressed shelving pulses after the Rydberg excitation which could potentially distort the result. On the

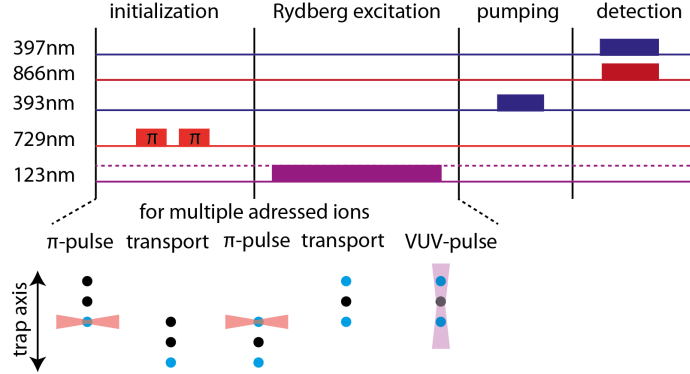


Figure 9. Pulse sequence for the Rydberg excitation and detection of selected ions. In case of addressed excitation of multiple ions, the ions are initialized serially, applying a transport sequence between each pulse. The following Rydberg excitation is done on all initialized ions at once.

downside, only 90% of the ground state population end up in the $3D_{5/2}$ state after pumping with light at 393 nm wavelength. While this only has a small effect for the addressed ions as they are predominantly in the $3D_{5/2}$ or $3D_{3/2}$ state at this point, it leads to a background of 10% for the non addressed ions to be in the 'bright' state. This effect is accounted for by adding 8% constant background to the data of the addressed ions.

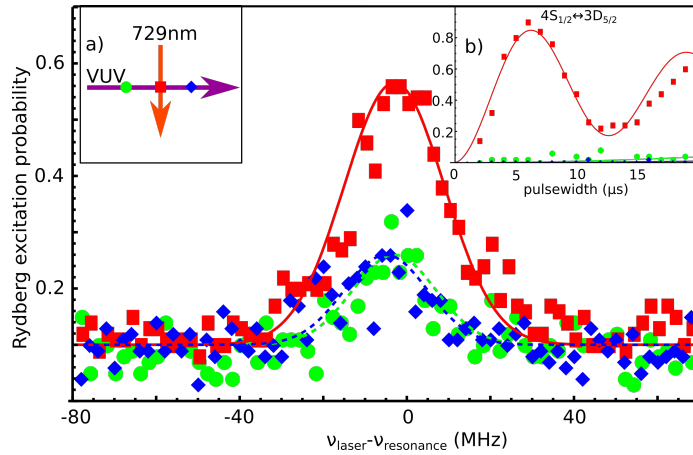


Figure 10. Addressed Rydberg excitation of the central ion out of a linear three ion crystal. The ratio for Rydberg excitation on the addressed to the non addressed ions is ≈ 3 with subtracted background signal. A constant background of 8% was added to the data of the addressed ion to account for this systematic error (see explanation in text). Inset a) shows the geometry of the beams with respect to the ion chain. Inset b) shows addressed Rabi oscillations on the $4S_{1/2} \leftrightarrow 3D_{5/2}$ transition. The population of the central ion flops at a frequency of $\Omega_{\text{Rabi}}/2\pi = 80$ kHz while the excitation of the outer ions remains negligible.

The measured resonance with central ion addressed is shown in Fig.10 the excitation rate on the addressed ion is about three times higher compared to the non

addressed ion. The Rabi oscillations on the $4S_{1/2} \leftrightarrow 3D_{5/2}$ transition are shown in inset b) of Fig. 10. During the time needed for a π -rotation on the addressed central ion, the excitation of the outer ions remains negligible. Still, residual Rydberg excitation of the non-addressed ions is observed. This behavior can be explained by the fact that we do not switch the VUV beam, but instead the VUV pulse width is determined by the time between initialization and detection. In contrast to the measurements presented in section 3.1, all ions (addressed and non-addressed) which have not been excited to Rydberg states are in the $3D_{5/2}$ state during detection. Consequently they can be excited during detection and decay to a bright state. Switching the VUV beam with an electro optical modulator should solve this problem and allow for better addressing fidelity limited only by the quality of the initialization.

Extending the scheme to the Rydberg excitation of multiple ions is straight forward. The measured resonance with outer ions addressed is presented in Fig. 11. In between laser pulses, the crystal is moved along the trap axis to superimpose the selected ion with the fixed 729 nm beam. Voltage ramps of $\Delta V = \pm 280$ mV on segments 4 and 8 have been used to displace the crystal by $14 \mu\text{m}$ in $500 \mu\text{s}$. In inset b) the Rabi oscillations on the $4S_{1/2} \leftrightarrow 3D_{5/2}$ transition are shown. Compared to the sequence for a single addressed ion, neither the contrast of the oscillation for the addressed ion is reduced, nor the unwanted excitation of the non-addressed ion is increased by the transport operations. In principle this approach is scalable to long ion chains and even to two dimensional ion crystals as long as Rydberg excitation is restricted to ions on the trap axis.

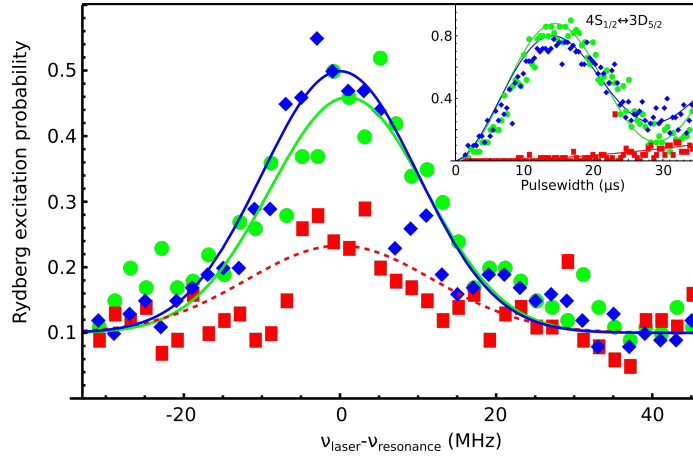


Figure 11. Addressed Rydberg excitation of both outer ions out of a linear three ion crystal. The ratio for Rydberg excitation on the addressed to the non addressed ions is ≈ 2.8 with subtracted background signal. Again, a constant background of 8% was added to the data of the addressed ions. The inset shows the coherent population transfer on the addressed $4S_{1/2} \leftrightarrow 3D_{5/2}$ transition. Even with pulses on both outer ions the excitation of the non-addressed central ions remains negligible. Compared to the data for a single addressed ion, no significant loss in fidelity is introduced by the transport operation.

4. Conclusion

In conclusion, we have extended the wavelength range of our VUV source in order to generate VUV radiation near 123 nm such that we are able to excite the Rydberg state $22F$. We combined the excitation of Rydberg ions in Paul traps with the coherent manipulation of the optical qubit in $^{40}\text{Ca}^+$ which is an important step towards quantum simulation and quantum information applications with Rydberg ions. As a side effect, we increased the detection efficiency of the Rydberg excitation by detecting changes in the magnetic quantum number m instead of the total angular momentum j . Using a segmented Paul trap, and the tightly focused beam at 729 nm as well as the VUV beam at 123 nm wavelength, we demonstrated the selective excitation of ions in a linear Coulomb crystal to Rydberg states.

However, the excitation of the $22F$ state is only an intermediate step as its lifetime, polarizability and dipole interaction between ions at a distance of a few μm would by far not allow Rydberg gate operations. We plan to excite long lived nP states near $n \approx 50$ in order to combine the toolbox of coherent qubit manipulations with the unique features of interacting Rydberg ions in Paul traps.

The authors thank M. Stappel, D. Kolbe and R. Gerritsma for helpful discussions. The work was funded by the European Union H2020 FET Proactive project RySQ (Grant No. 640378).

References

- [1] D. Leibfried, R. Blatt, C. Monroe, and D. Wineland, *Rev. Mod. Phys.* **75**, 281 (2003).
- [2] R. Blatt, and C. F. Roos, *Nature Physics* **8**, 277 (2012).
- [3] D. Kielpinski, C. Monroe, and D. J. Wineland, *Nature* **417**, 709 (2002).
- [4] J. I. Cirac, and P. Zoller, *Phys. Rev. Lett.* **74**, 4091 (1995).
- [5] T. Monz, D. Nigg, E. A. Martinez, M. F. Brandl, P. Schindler, R. Rines, S. X. Wang, I. L. Chuang, and R. Blatt, arXiv:1507.08852.
- [6] C. Senko, P. Richerme, J. Smith, A. Lee, I. Cohen, A. Retzker, and C. Monroe, *Phys. Rev. X* **5**, 021026 (2015).
- [7] P. Jurcevic, B. P. Lanyon, P. Hauke, C. Hempel, P. Zoller, R. Blatt, and C. F. Roos, *Nature* **511**, 202 (2014).
- [8] F. Schmidt-Kaler, H. Häffner, M. Riebe, S. Gulde, G. P. T. Lancaster, T. Deuschle, C. Becher, C. F. Roos, J. Eschner, and R. Blatt, *Nature* **422**, 408 (2003).
- [9] A. Sørensen, and K. Mølmer, *Phys. Rev. Lett.* **82**, 1971 (1999).
- [10] J. Benhelm, G. Kirchmair, C. F. Roos, and R. Blatt, *Nature Physics* **4**, 463 (2008).
- [11] D. Leibfried, B. DeMarco, V. Meyer, D. Lucas, M. Barret, J. Britton, W. M. Itano, B. Jelenkovic, C. Langer, T. Rosenband, and D. J. Wineland, *Nature* **422**, 412 (2003).
- [12] A. Gaëtan, Y. Miroshnychenko, T. Wilk, A. Chotia, M. Viteau, D. Comparat, P. Pillet, A. Browaeys, and P. Grangier, *Nature Physics* **5**, 115 (2009).
- [13] E. Urban, T. A. Johnson, T. Henage, L. Isenhower, D. D. Yavuz, T. G. Walker, and M. Saffman, *Nature Physics* **5**, 110 (2009).
- [14] L. Isenhower, E. Urban, X. L. Zhang, A. T. Gill, T. Henage, T. A. Johnson, T. G. Walker, and M. Saffman, *Phys. Rev. Lett.* **104**, 010503 (2010).
- [15] K. M. Maller, M. T. Lichtman, T. Sia, Y. Sun, M. J. Piotrowicz, A. W. Carr, L. Isenhower, and M. Saffman, *Phys. Rev. A* **92**, 022336 (2015).
- [16] D. Barredo, H. Labuhn, S. Ravets, T. Lahaye, A. Browaeys, and C. S. Adams, *Phys. Rev. Lett.* **114**, 113002 (2015).
- [17] P. Schauß, J. Zeiher, T. Fukuhara, S. Hild, M. Cheneau, T. Macri, T. Pohl, I. Bloch, and C. Gross, *Science* **347**, 1455 (2015).
- [18] H. Schempp, G. Günter, S. Wüster, M. Weidemüller, and S. Whitlock, *Phys. Rev. Lett.* **115**, 093002 (2015).
- [19] W. Li, A. W. Glaetzle, R. Nath, and I. Lesanovsky, *Phys. Rev. A* **87**, 052304 (2013).
- [20] W. Li, and I. Lesanovsky, *Phys. Rev. Lett.* **108**, 023003 (2012).

- [21] R. Nath, M. Dalmonte, A. W. Glaetzle, P. Zoller, F. Schmidt-Kaler, and R. Gerritsma, *New Journal of Physics* **17** (2015).
- [22] H. C. Nägerl, D. Leibfried, H. Rohde, G. Thalhammer, J. Eschner, F. Schmidt-Kaler, and R. Blatt, *Phys. Rev. A* **60**, 145 (1999).
- [23] T. Feldker, P. Bachor, M. Stappel, D. Kolbe, R. Gerritsma, J. Walu, and F. Schmidt-Kaler, *Phys. Rev. Lett.* **115**, 173001 (2015).
- [24] G. Jacob, K. Groot-Berning, S. Wolf, S. Ulm, L. Couturier, U. G. Poschinger, F. Schmidt-Kaler, K. Singer, arxiv.org:1405.6480, (2014).
- [25] A. Walther, F. Ziesel, T. Ruster, S. T. Dawkins, K. Ott, M. Hettrich, K. Singer, F. Schmidt-Kaler, and U. Poschinger, *Phys. Rev. Lett.* **109**, 080501 (2012).
- [26] T. Ruster, C. Warschburger, H. Kaufmann, C. T. Schmiegelow, A. Walther, M. Hettrich, A. Pfister, V. Kaushal, F. Schmidt-Kaler, and U. G. Poschinger, *Phys. Rev. A* **90**, 033410 (2014).
- [27] T. Macha *Frequenzstabilisierung eines Titan-Saphir-Laser und Verbesserung von Qubits mit Ca⁺ - Ionen*, (Diploma thesis) Gutenberg Univ. Mainz (2012).
- [28] D. Kolbe, M. Scheid, and J. Walz, *Phys. Rev. Lett.* **109**, 063901 (2012).
- [29] R. Steinborn, A. Koglbauer, P. Bachor, T. Diehl, D. Kolbe, M. Stappel, and J. Walz, *Optics Express* **21**, 22693 (2013).
- [30] I. L. Glukhov, E. A. Nikitina, and V. D. Ovsiannikov, *Spectroscopy of Atoms and Molecules* **115**, 9 (2013).
- [31] A. Kreuter, C. Becher, G. P. T. Lancaster, A. B. Mundt, C. Russo, H. Häffner, C. Roos, W. Hänsel, F. Schmidt-Kaler, R. Blatt, and M. S. Safronova, *Phys. Rev. A* **71**, 032504 (2005).